X-Ray Scattering Measurements of Strong Ion-Ion Correlations in Shock-Compressed Aluminum

T. Ma, T. Döppner, R. W. Falcone, L. Fletcher, C. Fortmann, D. O. Gericke, O. L. Landen, H. J. Lee, A. Pak, J. Vorberger, K. Wünsch, and S. H. Glenzer

Phys. Rev. Lett. **110**, 065001 — Published 5 February 2013

DOI: 10.1103/PhysRevLett.110.065001

X-Ray Scattering Measurements of Strong Ion-Ion Correlations in Shock-Compressed Aluminum

T. Ma,[1] T. Döppner,[1] R. W. Falcone,[2] L. Fletcher,[2] C. Fortmann,[1,3] D. O. Gericke,[4] O. L. Landen,[1] H. J. Lee,[5] A. Pak,[1] J. Vorberger,[4] K. Wünsch,[4] and S. H. Glenzer[1]

[1]*Lawrence Livermore National Laboratory, Livermore, CA 94550, USA*
[2]*Physics Department, University of California, Berkeley, CA 94720, USA*
[3]*Department of Physics and Astronomy, University of California, Los Angeles, CA 90095, USA*
[4]*Centre for Fusion, Space and Astrophysics, Department of Physics, University of Warwick, Coventry CV4 7AL, United Kingdom*
[5]*Stanford Linear Accelerator Center, Menlo Park, CA 94309, USA*

The strong ion-ion correlation peak characteristic of warm dense matter (WDM) is observed for the first time using simultaneous angularly, temporally, and spectrally resolved x-ray scattering measurements in laser-driven shock-compressed aluminum. Laser-produced molybdenum x-ray line emission at an energy of 17.9 keV is employed to probe aluminum compressed to a density of $\rho > 8\,\mathrm{g/cm^3}$. We observe a well pronounced peak in the static structure factor at a wave number of $k = 4.0\,\mathring{A}^{-1}$. The measurements of the magnitude and position of this correlation peak are precise enough to test different theoretical models for the ion structure and show that only models taking the complex interaction in WDM into account agree with the data. This also demonstrates a new highly accurate diagnostic to directly measure the state of compression of warm dense matter.

PACS numbers: 52.50.Jm, 52.25.Os, 52.27.Gr, 52.65.Yy

The accurate characterization of material properties under extreme conditions is important for the understanding of high energy density states of matter, ranging from planetary interiors to capsule implosions for inertial confinement fusion (ICF). Typically, x-ray Thomson scattering (XRTS) experiments have been conducted on low-Z, moderately compressed materials. However, recent progress on the National Ignition Facility (NIF) has yielded more than 600-fold compression of ICF ablator materials [1, 2], and > 100 Mbar compression of tantalum, spurring intense interest in high energy XRTS with probe energies above 10 keV to make it possible to penetrate and characterize these very dense states of matter.

Aluminum, a well-studied mid-Z element [3–8], serves as an excellent material for which to validate theoretical models that predict strong correlations very different from the ideal or weakly coupled plasma behavior, and which are expected in the warm dense matter regime [9, 10]. XRTS has been shown to robustly provide direct and accurate measurements of thermodynamic and transport properties, and can be applied as a non-invasive first principles technique to determine plasma temperature and density [11–13]. The extensive momentum-resolution of spectrally and angularly resolved XRTS presented here has not previously been used in WDM research and is critically needed to test details of dense plasma modeling.

In this Letter, we present high-energy x-ray scattering experiments in which tailored shocks are driven into solid aluminum targets to induce high compression (threefold solid density). Then, molybdenum 2p→1s x-ray line emission centered at 17.9 keV is used as a probe to penetrate the dense aluminum and perform scattering in the non-collective regime over a wide range of scattering angles. This high-energy, angularly resolved XRTS technique probes the ion-ion correlation peak, allowing for the unambiguous observation of a correlation peak with amplitude > 100, firmly in the strongly coupled plasma limit (high Γ). For the first time, these measurements are precise enough to allow the testing of different theoretical models and their predictions for the ion structure. We find that the usual plasma theories employing a linear screened Coulomb potential are insufficient to predict the magnitude of this correlation peak, and only calculations using a potential with additional short range repulsion can correctly fit the data. This work also directly demonstrates a novel diagnostic capability to measure the state of compression of a material with high accuracy.

From momentum and energy conservation, and the angle at which x-rays scatter from electrons, the dynamic structure factor is probed at various wave vectors $\mathbf{k}$, given by,

$$k = |\mathbf{k}| = \frac{4\pi E_0}{hc} \sin\frac{\theta_s}{2} \tag{1}$$

where $E_0 = 17.9\,\mathrm{keV}$ is the incident energy of the x-rays applied here, θ_s is the scattering angle, h is Planck's constant and c the speed of light. Such Thomson scattering [14] is characterized by the scattering parameter α,

$$\alpha = \frac{1}{k\lambda_s} \tag{2}$$

where λ_s is the screening length. In the non-degenerate case, λ_s is the standard Debye screening length, but in degenerate systems (as in this experiment) it is the Thomas-Fermi screening length. Here, both forward

and backward scattering is used to achieve scattering angles from 25° to 130° (comprising wave numbers of $4.0\,\text{Å}^{-1} < k < 16.4\,\text{Å}^{-1}$), and corresponding to a scattering parameter α in the interval $0.12 < \alpha < 0.52$, which indicates non-collective scattering.

The full spectral x-ray scattering response [15, 16] can be described by the total electron dynamic structure factor, which allows the following decomposition

$$S(k,\omega) = |f(k)+q(k)|^2 S_{ii}(k)\delta(\omega) + Z_f S_{ee}(k,\omega) + Z_C \int S_{CE}(k,\omega-\omega')S_S(k,\omega')d\omega' \,. \tag{3}$$

Here, $f(k)$ is the ion form factor, $q(k)$ describes the screening cloud, $S_{ii}(k)$ is the static ion structure factor and $S_{ee}(k,\omega)$ is the dynamic structure factor of the free electrons in the system. The response of the bound electrons in the system is described in part by the first term of Eq. (3) where the ion form factor is convolved with the ion structure factor. The free electrons in the system are responsible for two features in the total dynamic structure factor: first, the forming of a dynamic screening cloud around the ions is described by the product of $q(k)$ and the static ion structure; second, the spectral feature of free electrons totally independent of any ionic structure, described by the free electron dynamic structure factor. The latter contribution is determined by individual free electrons or collective electronic excitation (plasmons) depending on α. The third term includes inelastic scattering by bound electrons, i.e., bound-free transitions [17].

In the non-collective (Compton scattering) regime, the x-ray scattering spectrum is reflective of the individual electron motion, where the free electrons determine the broadening of the inelastic scattering component. The shift of the Compton peak is determined by the Compton energy $E_C = (hk/2\pi)^2/2m_e$, which in this experiment spans from 60 eV to 1.2 keV. In addition, the bound electrons with ionization energies larger than $h\omega/2\pi$ (states deep in the Fermi sphere) cannot be excited and elastically scatter. At large scattering vectors, the contribution from electrons in the screening cloud is negligible ($q(k)$ converges to 0) and the strength of the elastic scattering feature approaches $f(k)^2 S_{ii}$.

We performed the experiment on the OMEGA-60 laser at the Laboratory for Laser Energetics [18]. Fig. 1(a) shows a schematic of the experiment. The 125 μm thick aluminum foil targets are compressed from one side with a single strong shock generated using nine laser beams with a total energy of 4.5 kJ in a 1 ns square pulse. Distributed phase plates are used to achieve a smooth $\sim$ 1 mm focal spot, yielding a total drive intensity of 9×10^{14} W/cm^2 on the sample. 2-D radiation-hydrodynamic calculations using the HYDRA code [19] indicate this laser configuration launches a strong shock wave into the solid target, compressing the aluminum to more than threefold solid density with pressures of 30 − 40 Mbar. Bright, penetrating 17.9 keV Mo 2p→1s transition x-rays are used to probe the compressed Al at approximately 3.0 ns (matched to the shock propagation time to achieve uniform compression throughout the sample). These Mo x-rays are produced using 15 beams of 1 ns duration with an 80 μm focal spot, 500 J per beam, incident on a thin 12 μm molybdenum foil. To enhance the conversion efficiency into Mo thermal line radiation [20, 21], a single laser beam defocused to a 200 μm focal spot, 1 ns duration precedes the group of 15 beams by 1 ns to produce a low-density pre-plasma. The laser-to-Mo K-shell x-ray energy conversion efficiency is measured to be $1 - 2 \times 10^{-5}$.

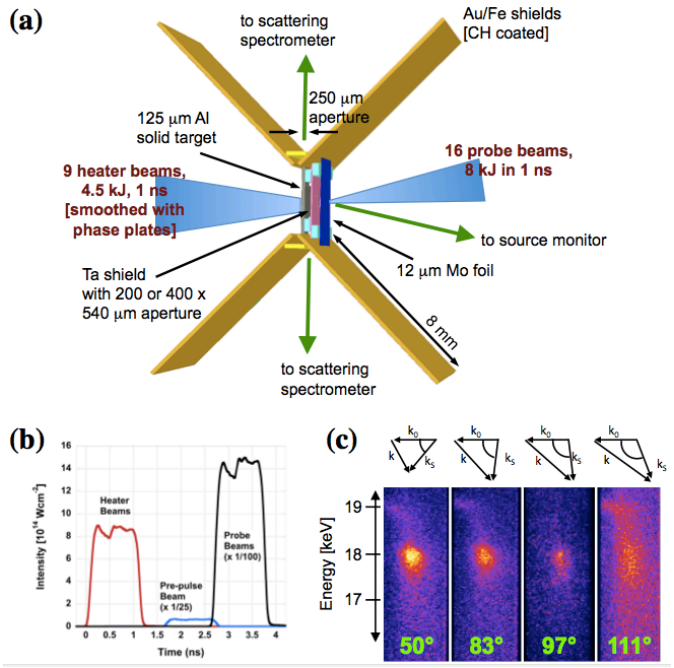

FIG. 1. (a) Schematic of the experiment showing nine heater beams that compress the Al foil and 16 delayed probe beams that produce $E = 17.9$ keV x-rays. X-ray scattering are observed in both the upward and downward directions with gated curved crystal spectrometers. The vertical location of the aperture in the Ta shield defines the two scattering angles on a given shot. (b) Heater, probe, and probe pre-pulse beam intensities on target. (c) Example of the raw scattering data show that the relative intensity of scattering is broadened and greatly reduced with increasing angle.

Tantalum apertures of either $200 \times 540\,\mu$m or $400 \times 540\,\mu$m between the molybdenum and aluminum foils (halfway between both, at a distance of 250 μm from each) serve to determine the range of k-vectors probed by selecting the solid angle subtended by the molybdenum x-rays. Furthermore, for any given shot, the vertical location of the aperture is moved relative to the source of molybdenum probe x-rays to change the incident probe radiation intersecting the shocked region, thus allowing for different scattering angles. For this experiment, the angular width of the probe beam typically encompasses $\sim 20°$, with the probe solid angle subtended at the sample of ~ 3 sr.

Large gold foils prevent the direct observation of the Mo plasma emission by two curved highly oriented pyrolytic graphite (HOPG) spectrometers [22]. Each of the two HOPG crystals used in the spectrometers that observe the scattering have a radius of curvature of 27 mm and are run in second order, giving a spectral resolution of $\lambda/\Delta\lambda \sim 175$ for the spectrum centered around the Mo He-α. The spectrometers are coupled to a microchannel-plate-based gated framing camera with 250 ps temporal resolution. The instrumental width of the scattered x-rays is determined to be $\sim$ 325 eV, dominated by the broad spectral feature comprised of thermally-driven Mo intercombination lines around 17.9 keV.

An absolutely calibrated Transmission Crystal Spectrometer [23, 24] monitors the output of the probe source in first order on each shot. The shot-to-shot variation in x-ray intensity of the Mo K-shell source centered at 17.9 keV is found not to vary by more than 13%, which is taken into account for comparing signal levels from different shots.

An example of the raw scattering data recorded at several scattering angles is shown in Fig. 1(c). The observed total signal is dominated by the elastically scattered photons and shows a strong dependence on the angle of scatter.

Figure 2 shows two examples of the spectrally resolved scattering spectra for 69° ($k = 10.3\,\mathring{A}^{-1}$) and 111° ($k = 15.0\,\mathring{A}^{-1}$). The experimental spectra are background corrected and smoothed over 100 eV. Also shown are the best fits from synthetic spectra generated by convolving Eq. (3) with the experimental instrument function. The individual contributions from elastic, free-free, and bound-free scattering are illustrated. The free electron feature is derived within the random phase approximation [25] and the elastic amplitude is fitted for comparison with detailed theories [26]. For small scattering angles ($25° < \theta_s < 50°$), the total frequency resolved scattering spectrum reflects the source spectrum. For the full set of experimental scattering spectra taken at the various scattering angles, good theoretical fits were found at a mass density of $\rho = 8.1\,\mathrm{g/cm^3}$, electron and ion temperatures of $T_e = T_i = 10$ eV, and an average ioniziation state of $Z = 3$. These values are in agreement with the HYDRA radiation-hydrodynamic modeling.

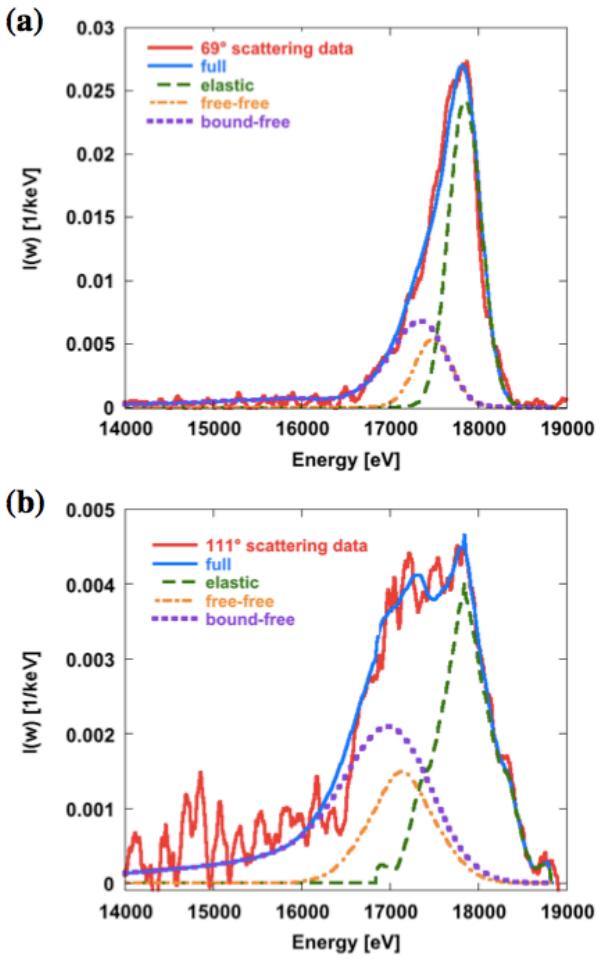

FIG. 2. Examples of x-ray scattering spectra from singly shocked Al for two different scattering angles. Best fit for the $\theta = 69°$ (a) and 111° (b) experimental data together with the individual contribution from elastic scattering corresponding to the first term in Eq. (3), inelastic scattering from free electrons (free-free scattering) corresponding to the second term in Eq. (3), and inelastic scattering from bound electrons (bound-free scattering) corresponding to the third term in Eq. (3). The full synthetic x-ray scattering spectrum takes into account the sum of these contributions. The experimental spectra have been background corrected and are plotted in absolute units of intensity of the dynamic structure factor.

The width of the downscattered inelastic feature is responsive to the relative contributions of the bound-free and free-free feature, which is utilized to infer the number of bound electrons and hence the ionization degree of the plasma. Because the plasma is Fermi-degenerate ($T_e < T_F$), the scattering parameter, α, depends only weakly on the electron density ($\sim n_e^{1/6}$), and is independent of T_e. Thus, the relative intensity ratio between the elastic and inelastic scattering features is almost uniquely a function of the number of free electrons (modifying the

screening). For these spectral fits, the bound-free profiles are treated with the form factor approximation (FFA). While the balance between the bound-free and free-free components will alter slightly based on the bound-free model chosen, the total intensity of the inelastic feature will not change. The fits here are consistent with a Z of 3.

The absolute intensity of the total electron dynamic structure factor is determined from the integral of the spectrally resolved XRTS spectrum for each scattering angle. Corrections are made to the measured scattered power for the polarization of the incident radiation and the length and solid angle of the scattering volume. To obtain absolute calibration, the first frequency moment (f-sum rule) [25] is applied to the 111° data (a high k case where the Compton shift is considerable enough to separate the elastic from the inelastic peak) to derive a calibration constant. The amplitude of the elastic scattering is then determined by subtracting out the free-free and bound-free components. The free-free contribution is directly calculated from the scaling $S_{ee} \propto 1/(1+\alpha^2)$, and the contribution from bound-free transitions is analytically derived as described in Ref. [16].

Figure 3 shows the measured strength of the elastic scattering signal, $W_R(k) = [f(k)+q(k)]^2 S_{ii}(k)$, as a function of scattering vector k for shock-compressed aluminum with $\rho = 8.1\,\mathrm{g/cm^3}$ and $T_e = T_i = 10\,\mathrm{eV}$ at 13 different wave numbers (or scattering angles). A sharp maximum of $W_R(k) = 106$ is exhibited at $k = 4.0\,\mathring{A}^{-1}$, a compelling indication of the strongly coupled state of the shocked aluminum. Previous measurements of the elastic scattering intensity were only achieved in low Z materials (e.g., in LiH at much lower pressures of $3-4$ Mbar [27]), near the plasma limit, with peak elastic scattering amplitudes below 1.5.

We model the weight of the Rayleigh peak using four different approaches: the Debye-Hueckel (DH) model [26], the screened one component plasma (SOCP) model [26], and via the Ornstein-Zernicke equation using the HNC closure together with a potential incorporating linear screening (Yukawa, HNC-Y) and HNC calculations applying a potential with an additional short range repulsion (HNC-Y+SRR) [10]. All models incorporate a $\pm 10°$ k-vector blurring for each angle considered, consistent with the geometry of the experiment. Analytical calculations in the form of the DH model, derived for weakly coupled plasmas naturally fail to capture the clear trend seen in the experimental data, as the DH model cannot describe the strong ion-ion correlations. The SOCP and HNC-Y models, which assume ions are embedded in a polarizable electron gas and, thus, interact via a screened Coulomb potential, predict a pronounced peak at the right location, with an approximate width of the peak of the correct span, but underestimate the absolute amplitude of the correlation peak. Although both models aim to include similar physics, technical differences

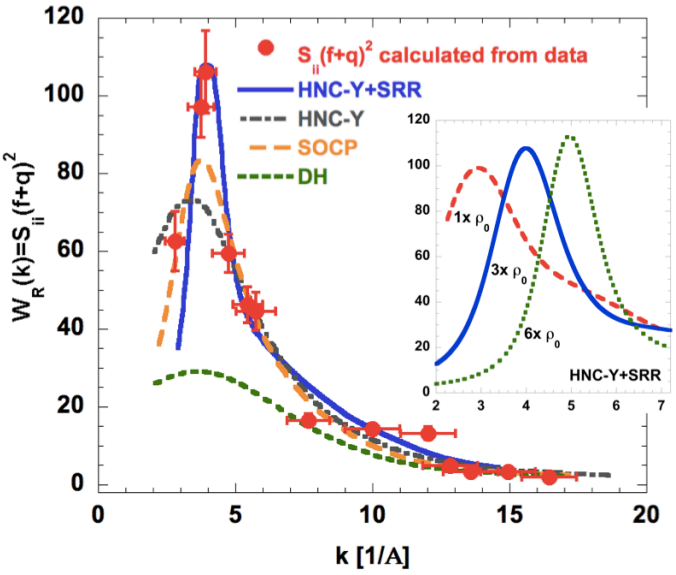

FIG. 3. Elastic scattering amplitude data measured as a function of scattering vector $\mathbf{k}$ from shock-compressed aluminum for a density of $n_e = 5.4\times10^{23}\,\mathrm{cm^{-3}}$ and temperature $T_e = 10\,\mathrm{eV}$. Also shown are various calculations using HNC with quantum potential models of [10] and the analytical SOCP and DH models of [26]. Inset: The shift and change in peak intensity of the correlation peak for uncompressed, 3×, and 6× compressed aluminum (at $T_e = 10\,\mathrm{eV}$), modeled using HNC-Y+SRR, can serve as a density diagnostic.

typically arise for strong coupling [28] as investigated here. Only the most advanced model, HNC-Y+SRR, which explicitly accounts for the complex strong interactions in WDM, agrees with the data. This demonstrates the importance of the short range repulsion stemming from bound electrons in addition to Yukawa-type linear screening caused by the free electrons.

These calculations also show that the elastic x-ray scattering amplitude peak shifts to higher wave number and larger peak intensity with increasing degree of compression (inset, Fig. 3). By doubling the density of the Al (as can be done in a counter propagating shock collision), the ion-ion correlation peak is expected to shift by $\Delta k = 1\,\mathring{A}^{-1}$, corresponding to $\Delta\theta = 10°$ in the geometry used in this experiment. As temperature and ionization of the Al material are varied, the position of the maximum does not vary significantly, but the width of the peak changes. This presents a new diagnostic opportunity to characterize compressed states of matter by wave number resolving the elastic amplitude to complement the findings from the frequency resolved inelastic scattering.

In summary, we have used angularly resolved x-ray Thomson scattering at 17.9 keV over a very wide range of wave vectors to probe a compressed mid-Z material. The experimental data show a strong correlation peak characteristic of the warm dense matter state. For the

first time, the measurements of the scattering are precise enough to distinguish between theoretical models for the ion structure and show that screening effects must be accounted for in order to fit the shape and absolute intensity of the data. This demonstrates the capability of XRTS to resolve the ion-ion correlation for an accurate measurement of compression.

This work was performed under the auspices of the U.S. Department of Energy by Lawrence Livermore National Laboratory under Contract DE-AC52-07NA27344. Work was also supported by the Laboratory Directed Research and Development Grant 11-ERD-050 and the National Laboratory User Facility.

[1] M. J. Edwards, J. D. Lindl, B. K. Spears, S. V. Weber, L. J. Atherton, D. L. Bleuel, D. K. Bradley, D. A. Callahan, C. J. Cerjan, D. Clark, et al., Physics Of Plasmas **18**, 051003 (2011).

[2] S. H. Glenzer, D. A. Callahan, A. J. Mackinnon, J. L. Kline, G. Grim, E. T. Alger, R. L. Berger, L. A. Bernstein, R. Betti, D. L. Bleuel, et al., Physics Of Plasmas **19**, 056318 (2012).

[3] D. Riley, N. Woolsey, D. McSherry, I. Weaver, A. Djaoui, and E. Nardi, Physical Review Letters **84**, 1704 (2000).

[4] A. Ravasio, G. Gregori, A. Benuzzi-Mounaix, J. Daligault, A. Delserieys, A. Faenov, B. Loupias, N. Ozaki, M. R. Le Gloahec, T. Pikuz, et al., Physical Review Letters **99**, 135006 (2007).

[5] E. García Saiz, G. G. Gregori, F. Y. F. Khattak, J. J. Kohanoff, S. S. Sahoo, G. S. G. Naz, S. S. Bandyopadhyay, M. M. Notley, R. L. R. Weber, and D. D. Riley, Physical Review Letters **101**, 075003 (2008).

[6] B. Nagler, U. Zastrau, R. Fäustlin, S. Vinko, T. Whitcher, A. Nelson, R. Sobierajski, J. Krzywinski, J. Chalupsky, E. Abreu, et al., Nature Physics **5**, 693 (2009).

[7] H. Sawada, S. P. Regan, P. B. Radha, R. Epstein, D. Li, V. N. Goncharov, S. X. Hu, D. D. Meyerhofer, J. A. Delettrez, P. A. Jaanimagi, et al., Physics Of Plasmas **16**, 052702 (2009).

[8] O. Ciricosta, S. Vinko, H. K. Chung, B. I. Cho, C. Brown, T. Burian, J. Chalupsky, K. Engelhorn, R. Falcone, C. Graves, et al., Physical Review Letters **109**, 065002 (2012).

[9] K. Wünsch, P. Hilse, M. Schlanges, and D. O. Gericke, Physical Review E **77**, 056404 (2008).

[10] K. Wünsch, J. Vorberger, and D. O. Gericke, Physical Review E **79**, 010201 (2009).

[11] S. Glenzer, G. Gregori, R. Lee, F. Rogers, S. Pollaine, and O. Landen, Physical Review Letters **90**, 175002 (2003).

[12] H. J. Lee, P. Neumayer, J. Castor, T. Döppner, R. W. Falcone, C. Fortmann, B. A. Hammel, A. L. Kritcher, O. L. Landen, R. W. Lee, et al., Physical Review Letters **102**, 115001 (2009).

[13] C. Fortmann, H. Lee, T. Döppner, R. Falcone, A. Kritcher, O. Landen, and S. Glenzer, Physical Review Letters **108**, 175006 (2012).

[14] S. H. Glenzer and R. Redmer, Reviews of Modern Physics **81**, 1625 (2009).

[15] J. Chihara, Journal of Physics: Condensed Matter **12**, 231 (2000).

[16] G. Gregori, S. Glenzer, W. Rozmus, R. Lee, and O. Landen, Physical Review E **67**, 026412 (2003).

[17] B. Mattern, G. Seidler, J. Kas, J. Pacold, and J. Rehr, Physical Review B **85** (2012).

[18] T. R. Boehly, R. S. Craxton, T. H. Hinterman, J. H. Kelly, T. J. Kessler, S. A. Kumpan, S. A. Letzring, R. L. Mccrory, S. F. B. Morse, W. Seka, et al., Review of Scientific Instruments **66**, 508 (1995).

[19] M. M. Marinak, G. D. Kerbel, N. A. Gentile, O. Jones, D. Munro, S. Pollaine, T. R. Dittrich, and S. W. Haan, Physics Of Plasmas **8**, 2275 (2001).

[20] K. Fournier, J. Satcher, M. May, J. Poco, C. Sorce, J. Colvin, S. B. Hansen, S. MacLaren, S. Moon, and J. Davis, Physics Of Plasmas **16**, 052703 (2009).

[21] F. Girard, J. P. Jadaud, M. Naudy, B. Villette, D. Babonneau, M. Primout, M. C. Miller, R. L. Kauffman, L. J. Suter, J. Grun, et al., Physics Of Plasmas **12**, 092705 (2005).

[22] A. Pak, G. Gregori, J. Knight, K. Campbell, D. F. Price, B. Hammel, O. L. Landen, and S. H. Glenzer, Review of Scientific Instruments **75**, 3747 (2004).

[23] J. Seely, G. Holland, L. Hudson, C. Szabo, A. Henins, H. S. Park, P. K. Patel, R. Tommasini, and J. Martinlaming, High Energy Density Physics **3**, 263 (2007).

[24] C. Szabo, U. Feldman, S. Seltzer, L. Hudson, M. O'Brien, H. Park, and J. Seely, Optics Letters **36**, 1335 (2011).

[25] S. Ichimaru, Reviews of Modern Physics **54**, 1017 (1982).

[26] G. Gregori, A. Ravasio, A. Höll, S. Glenzer, and S. Rose, High Energy Density Physics **3**, 99 (2007).

[27] A. L. Kritcher, P. Neumayer, C. R. D. Brown, P. Davis, T. Döppner, R. W. Falcone, D. O. Gericke, G. Gregori, B. Holst, O. L. Landen, et al., Physical Review Letters **103**, 245004 (2009).

[28] K. Wünsch, J. Vorberger, G. Gregori, and D. O. Gericke, Journal of Physics A: Mathematical and Theoretical **42**, 214053 (2009).